Embedded Peierls instability and the electronic structure of MoO$_2$

Embedded Peierls instability and the electronic structure of MoO₂

V Eyert†, R Horny, K-H Höck and S Horn

Institut für Physik, Universität Augsburg, 86135 Augsburg, Germany

Abstract. Molybdenum dioxide crystallizes in a monoclinic structure which deviates only slightly from the rutile structure and is characteristic of several early transition metal dioxides. We present results of all-electron electronic structure calculations based on density functional theory within the local density approximation and using the augmented spherical wave method. The electronic properties of MoO_2 are dominated by strong hybridization of O 2p and crystal-field-split Mo 4d states with bands near the Fermi energy originating almost exclusively from Mo 4d t_{2g} orbitals. In additional calculations for a hypothetical high-symmetry rutile structure these bands separate into quasi-one-dimensional $d_\parallel$ states pointing along the rutile c-axis and the rather isotropically dispersing π^* bands. On going to the monoclinic structure, the characteristic metal–metal dimerization causes strong splitting of the $d_\parallel$ bands into bonding and antibonding branches which embrace the nearly inert π^* bands at E_F. As a consequence, large portions of the Fermi surface are removed. According to our calculations the monoclinic structure of MoO_2 thus results from a Peierls-type instability of the $d_\parallel$ bands in the presence of, but still rather unaffected by, an embedding background of π^* states. Our work has strong implications for the current understanding of VO_2 and the striking metal–insulator/structural transition displayed by this material.

1. Introduction

The rutile-related transition metal dioxides have long been attracting a lot of attention due to a large variety of physical phenomena arising from the hybridization of the narrow d states with the ligand p orbitals [1]. This diversity shows up mainly in the 3d series which comprises the large-gap semiconductor TiO_2, the half-metallic ferromagnet CrO_2, and the antiferromagnetic semiconductor MnO_2 [2, 3], whereas most of the 4d and 5d compounds are neither semiconducting nor magnetic. However, there exist several members in each group which display small but characteristic deviations from the rutile structure [1, 2, 4].

Among the transition metal dioxides the d^1 members VO_2 and NbO_2 are exceptional since they both undergo a metal–insulator transition which is accompanied by a structural transition from the high-temperature rutile phase to a low-temperature low-symmetry phase. The change in resistivity especially for vanadium dioxide extends over several orders of magnitude and, occurring at 340 K, led researchers to expect a broad range of applications [5]. Nevertheless, the origin of the metal–insulator transition is still a matter of controversy. Several models have been proposed emphasizing either electron–phonon coupling or strong electron–electron correlations as the driving force. As a consequence, a complete and widely accepted picture of the physics of the rutile-related transition metal oxides has not yet evolved.

† Homepage: http://www.physik.uni-augsburg.de/˜eyert/.

In fact, the deviations from the rutile structure, if present, are of the same kind for all the early transition metal dioxides. To be specific, MoO_2, WO_2, TcO_2, α-ReO_2, and low-temperature VO_2 crystallize in a structure with monoclinic space group and exhibiting the same characteristics as the rutile structure, namely, a pairing of the metal atoms parallel to the rutile c-axis and a lateral, zigzag-like, displacement [1]. In contrast, insulating NbO_2, while displaying the same local shifts of the metal atoms, crystallizes in a body-centred lattice with 32 formula units per cell [6, 8–10]. Thus, to get an idea of the general tendency of the rutile-type transition metal dioxides to crystallize in a low-symmetry structure as well as of the impact of the structural properties on the metal–insulator transition, it is worthwhile to look at compounds neighbouring VO_2 which display the same distortion but no such transition. A possible candidate is MoO_2, which is metallic and shows neither a metal–insulator nor a structural phase transition [1]. Effective masses similar to the free-electron mass have been reported for this material [17, 18, 21], which, hence, is regarded as rather uncorrelated [7]. It is thus expected, that, by investigating molybdenum dioxide, we might be able to determine factors which govern the stability of the monoclinic phase, without being faced with the effects of electron correlations. Naturally, this will have a considerable impact on our understanding of the neighbouring compounds and, in particular, of the metal–insulator transitions of VO_2 and NbO_2.

The electronic structure of MoO_2 has been investigated theoretically by means of phenomenological molecular orbital schemes as well as tight-binding and cluster calculations [1, 22–27], whereas state-of-the-art band calculations for the crystalline material are still lacking. According to optical reflectivity measurements, the lowest unfilled Mo 4d levels lie about 2.5 eV above the top of the O 2p bands [11, 12]. UPS and XPS experiments revealed an approximately 9 eV wide occupied band falling into the low-binding, 3 eV wide Mo 4d bands and a 6 eV wide group of O 2p bands at higher binding energies [13–15]. The Mo 4d bands further split into a doublet with peaks at 1.5 and 0.5 eV below the Fermi energy [13, 15]. The unoccupied O 2p states, in contrast, as measured by XAS experiments, fall into three peaks at 1.4, 3.1, and 4.6 eV above the Fermi energy [16]. Finally, de Haas–van Alphen and Shubnikov–de Haas measurements revealed marked anisotropies of the Fermi surface [17–21].

In the present study we aim at a comprehensive characterization of the electronic structure in terms of a few relevant orbitals. Furthermore, in order to investigate the mechanisms which force some of the dioxides into distorted variants of the rutile structure, we complement the calculations for the experimentally determined monoclinic structure with an additional set of calculations which use a hypothetical rutile cell arising from symmetrization of the monoclinic structure. This serves two purposes:

(i) The results for hypothetical rutile MoO_2 establish a reference, to which the electronic structure of 'real' MoO_2 can be compared. From the differences between the two sets of calculations, information concerning the stability of the monoclinic structure can be deduced.

(ii) Investigation of the rutile system in itself might allow one to identify mechanisms which would destabilize the rutile phase and make MoO_2 monoclinic. This includes a closer look at the Fermi surface as calculated with the hypothetical rutile structure.

The paper is organized as follows. Starting with a short description of the monoclinic crystal structure and its relation to the rutile structure in section 2, we outline the calculational method in section 3. The results are presented and discussed in section 4 and summarized in section 5.

2. Crystal structure

MoO$_2$ crystallizes in a simple monoclinic lattice with space group $P2_1/c$ (C_{2h}^5) [31, 32]. The lattice constants and the monoclinic angle amount to $a_M = 5.6109$ Å, $b_M = 4.8562$ Å, $c_M = 5.6285$ Å, and $\beta = 120.95°$, respectively [32]. The crystal structure is displayed in figure 1. The unit cell, which is highlighted by thick solid lines, comprises four formula units. The metal atoms as well as the two inequivalent oxygen atoms occupy the general Wyckoff positions (4e): $\pm(x, y, z)$, $\pm(x, \frac{1}{2} - y, \frac{1}{2} + z)$ with the parameters listed in table 1. We have adopted the standard notation

$$a_{M1} = \begin{pmatrix} 0 \\ 0 \\ -a_M \end{pmatrix} \qquad a_{M2} = \begin{pmatrix} -b_M \\ 0 \\ 0 \end{pmatrix} \qquad a_{M3} = \begin{pmatrix} 0 \\ c_M \sin\beta \\ -c_M \cos\beta \end{pmatrix} \qquad (1)$$
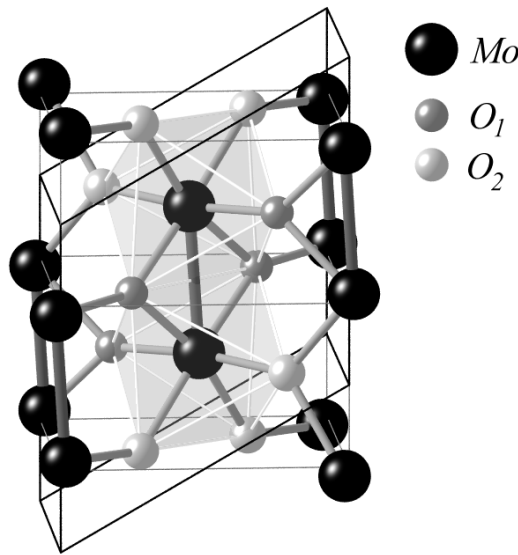
for the primitive translations.

Figure 1. The crystal structure of monoclinic MoO$_2$.

Table 1. Crystal structure parameters of monoclinic MoO$_2$ (from reference [32]).

Atom	Wyckoff positions	Parameters		
		x	y	z
Mo	(4e)	0.2316	−0.0084	0.0164
O$_1$	(4e)	0.1123	0.2171	0.2335
O$_2$	(4e)	0.3908	−0.3031	0.2987

The close relationship of the monoclinic crystal structure with the rutile structure is still visible in figure 1, where, apart from the atomic displacements to be discussed below, the atoms form two stacked rutile cells as indicated by the thin solid lines. Note that the corners of the monoclinic and tetragonal cells are shifted by half the rutile c-axis or by quarter of the monoclinic a-axis, which causes the shift of the x-components of all positions in table 1 by 0.25. The rutile structure is based on a simple tetragonal lattice with space group $P4_2/mnm$

(D_{4h}^{14}) [30]. The metal atoms are located at the Wyckoff positions (2a): $(0, 0, 0)$, $(\frac{1}{2}, \frac{1}{2}, \frac{1}{2})$, and the oxygen atoms occupy the positions (4f): $\pm(u, u, 0)$, $\pm(\frac{1}{2} + u, \frac{1}{2} - u, \frac{1}{2})$. Yet, the rutile structure can be alternatively visualized in terms of a body-centred tetragonal lattice formed by the metal atoms where each metal is surrounded by an oxygen octahedron. Octahedra centred at the corners and the centre of the cell are rotated by $90°$ about the tetragonal c-axis relative to each other. As a consequence, the lattice translational symmetry reduces to simple tetragonal and a unit cell with two formula units results. Octahedra which are neighbouring along the rutile c-axis share edges, whereas the resulting octahedral chains are interlinked via corners. Each octahedron has orthorhombic symmetry although the deviations from tetragonal and even cubic geometry for most compounds are relatively small and still allow for a discussion in terms of the latter. There exist two different metal–oxygen distances, namely, the apical distance, which is between metal and oxygen atoms having the same z-value, and the equatorial distance between the metal atom and the four neighbouring ligand atoms with $z = z_{\text{metal}} \pm 1/2$ [2,3,30].

Although there have been indications for the possible onset of a monoclinic-to-rutile transition at temperatures above 1100 °C for $Mo_{0.975}Ti_{0.025}O_2$ [33, 34], no structural phase transition has been reported for the stoichiometric compound. Nevertheless, since the monoclinic structure is closely related to the rutile structure, we may construct a hypothetical rutile cell by properly symmetrizing the atomic positions which will serve as a reference throughout this paper. As a result, we arrive at lattice constants of $a = 4.8562$ Å and $c = 2.80545$ Å, which are identical to the monoclinic lattice constants b_M and $a_M/2$, respectively [32]. The rather small c/a ratio of 0.5777 is a consequence of the metal–metal bonding along the rutile c-axis and is characteristic of the 4d and 5d d^2 and d^3 compounds [1]. Finally, the internal u-parameter of the rutile structure, which determines the oxygen position, assumes the value 0.2847. Note that while symmetrizing the monoclinic structure we have ignored the strain inherent in this lattice. For this reason, the lattice constants and the internal u-parameter of the symmetrized rutile cell still contain small uncertainties.

With the rutile reference structure at hand, the distinct deviations of the observed monoclinic structure from the hypothetical rutile structure are easily stated:

(i) We observe in figure 1 the aforementioned metal–metal pairing along the tetragonal c-axis. Due to the alternation of the vertical metal-atom displacements in the directions of the y-axis, the lattice is simple monoclinic rather than simple tetragonal with a double c-axis.

(ii) Slightly less marked are the in-plane displacements of the Mo atoms which make an angle of $18°$ with the local apical axis of each octahedron. These shifts likewise alternate along both the tetragonal a- and c-axes, thus causing the zigzag-like shape of the vertical metal chains. The oxygen atoms follow the *lateral* displacements of the metal atoms to a large degree, whereas the deviations of the *vertical* oxygen components from the ideal rutile values are much smaller.

(iii) There is a lattice strain which causes deviations from unity of the ratios

$$\frac{c_M \sin \beta}{b_M} = 0.9940 \qquad \frac{-2c_M \cos \beta}{a_M} = 1.0318.$$

It is useful to discuss the electronic structure of rutile-type compounds in terms of local coordinate systems centred at each metal site. This has been indicated in figure 2, where we display the angular parts of the metal d orbitals relative to the local reference frame of the central metal atom. Note that due to the different orientations of octahedra centred at the corner and the centre of the rutile cell, the local z-axes point alternately along the [110] and [1$\bar{1}$0] directions. In contrast to the usual adjustment of the x- and y-axes parallel to the metal–ligand bonds [30], we have rotated these axes by $45°$ about the local z-axes such that they are parallel and perpendicular, respectively, to the rutile c-axis. With this choice of local
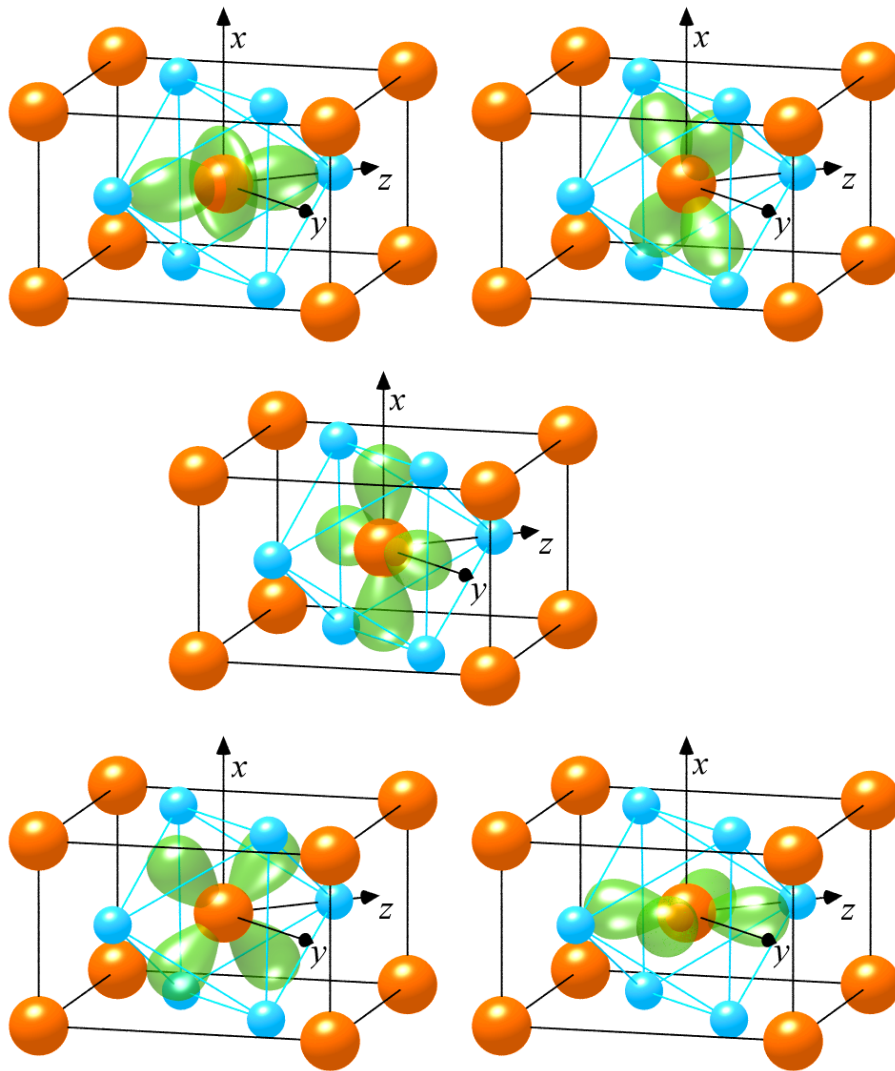
Figure 2. Angular parts of the d orbitals. Top: $d_{3z^2-r^2}$ and d_{xy}; middle: $d_{x^2-y^2}$; bottom: d_{xz} and d_{yz}.

coordinate systems the e_g states resulting from the cubic part of the crystal-field splitting of the metal d orbitals comprise the $d_{3z^2-r^2}$ and d_{xy} orbitals, whereas the t_{2g} states are made up of the $d_{x^2-y^2}$, d_{xz}, and d_{yz} orbitals. The $d_{x^2-y^2}$ orbitals point along the rutile c-axis and the local y-axes, i.e. towards the edges of the basal plane of the octahedron, while the d_{xz} and d_{yz} orbitals are directed towards the faces. In particular, the d_{yz} states point along the $\langle 100 \rangle$ directions. As a consequence, the $d_{x^2-y^2}$ and d_{xz} orbitals mediate σ- and π-type overlap, respectively, between metal sites within the vertical octahedron chains. The d_{yz} orbitals have a σ-type overlap, albeit smaller, with their counterparts at metal sites translated by the vectors $\langle 1, 0, 0 \rangle$. This is due to the aforementioned 45° rotation of the local coordinate system, which interchanges the $d_{x^2-y^2}$ and d_{xy} orbitals and adjusts the d_{yz} orbitals parallel to the axes of the rutile basal plane. While the overlap of both the $d_{x^2-y^2}$ and d_{yz} orbitals with orbitals of the

same kind at neighbouring atoms thus connects atoms which are separated by lattice vectors of the simple tetragonal lattice, coupling between metal atoms which are located at the corner and the centre of the cell is mediated by the d_{xz} orbitals. These orbitals point to the voids between the metal atoms of the neighbouring octahedral chains where they overlap with the $d_{x^2-y^2}$ orbitals of these chains.

3. Method of calculation

The calculations are based on density functional theory (DFT) and the local density approximation (LDA) [35, 36]. We employ the augmented spherical wave (ASW) method [37] in its scalar-relativistic implementation (see references [38–40] for more recent descriptions). Since the ASW method uses the atomic sphere approximation (ASA) [41], we had to insert so-called empty spheres into the open rutile structure. These empty spheres are pseudo-atoms without a nucleus, which are used to model the correct shape of the crystal potential in large voids [42]. In order to minimize the sphere overlap we have recently developed the sphere geometry optimization (SGO) method, which solves the problem of finding optimal empty-sphere positions as well as the radii of all spheres automatically [43]. The routine was applied to both the rutile and the monoclinic cell. For the former structure, with the addition of eight empty spheres, the linear overlap of any pair of physical spheres could be kept below 22%, and the overlap of any pair of physical and empty spheres below 25%. The positions of the empty spheres are listed in table 2. In addition to the empty-sphere positions, the SGO algorithm produced atomic sphere radii for all spheres, which are listed in table 3. Table 3 moreover supplies the orbitals used as the basis set for the present calculations. States given in parentheses were included as tails of the other orbitals (see references [37–40] for more details on the ASW method).

Table 2. Empty-sphere positions for hypothetical rutile MoO_2.

		Parameter
Atom	Wyckoff positions	x
E_1	(4c)	
E_2	(4g)	0.3497

Table 3. Atomic sphere radii and basis-set orbitals for hypothetical rutile MoO_2.

Atom	Radius/a_B		Orbitals		
Mo	2.330	5s	5p	4d	(4f)
O	2.138	2s	2p	(3d)	
E_1	1.741	1s	2p	(3d)	
E_2	1.740	1s	2p	(3d)	

For the monoclinic cell, twelve empty spheres were needed to keep the linear overlaps below 20% and 22%, respectively. The positions of the empty spheres as well as the sphere radii and orbitals are listed in tables 4 and 5.

Self-consistency was achieved by using an efficient algorithm for convergence acceleration [44]. The Brillouin zone sampling was done using an increased number of **k**-points ranging from 18 to 1800 points and from 54 to 6750 points, respectively, within the irreducible

Table 4. Empty-sphere positions for monoclinic MoO_2.

Atom	Wyckoff positions	Parameters		
		x	y	z
E_1	(2d)	0.5	0.5	0.0
E_2	(2c)	0.0	0.0	0.5
E_3	(4e)	0.3458	0.3754	0.1805
E_4	(4e)	0.1544	−0.1070	0.3110

Table 5. Atomic sphere radii and basis-set orbitals for monoclinic MoO_2.

Atom	Radius/a_B	Orbitals				
Mo	2.600	5s	5p	4d	4f	(5g)
O_1	1.650	2s	2p	(3d)		
O_2	1.843	2s	2p	(3d)		
E_1	2.197	1s	2p	3d	(4f)	
E_2	2.372	1s	2p	3d	(4f)	
E_3	1.908	1s	2p	3d	(4f)	
E_4	1.788	1s	2p	(3d)		

wedge of the tetragonal and monoclinic lattices, ensuring convergence of our results with respect to the fineness of the **k**-space grid.

In addition to the band structure and the (partial) densities of states, we evaluated the crystal orbital overlap population (COOP) based on the notions introduced by Hoffmann [28] in order to allow for a discussion of chemical bonding. The evaluation of the COOP has been recently implemented in the ASW method [29] (see also references [3,45]); it was successfully applied to the interpretation of bonding properties of various compounds [3].

4. Results and discussion

4.1. Band structure and density of states

Within a molecular orbital picture we expect the oxygen 2p levels to be completely filled and the Mo 4d levels to comprise two electrons. Due to the orthorhombic rather than cubic symmetry of the octahedra surrounding the metal sites, the low-lying t_{2g} and the high-lying e_g manifolds are further split into singlets. Yet, since the deviations from local cubic symmetry are small, the crystal-field splitting still should be dominated by its cubic part.

In presenting the calculated results we start out from the hypothetical rutile reference system and display in figure 3 the electronic states along selected high-symmetry lines within the first Brillouin zone of the simple tetragonal lattice, shown in figure 4(a). The corresponding density of states (DOS) is given in figure 5 where we have added the dominant partial densities of states. The total density of states at the Fermi energy, $N(E_F)$, amounts to 1.3 states eV^{-1}/f.u. Not shown are low-lying oxygen 2s states.

In figures 3 and 5 we identify three groups of bands. In the energy range from −9.2 to −3.6 eV we observe twelve bands, which trace back mainly to O 2p states but have a non-negligible contribution due to the Mo 4d states. Bands are most easily counted along the direction X–R where they are twofold degenerate. The upper two groups, which extend from −2 to 2.7 and from 3.1 to 6.8 eV, contain six and four bands, respectively, and originate mainly from Mo 4d states. However, p–d hybridization causes additional O 2p contributions
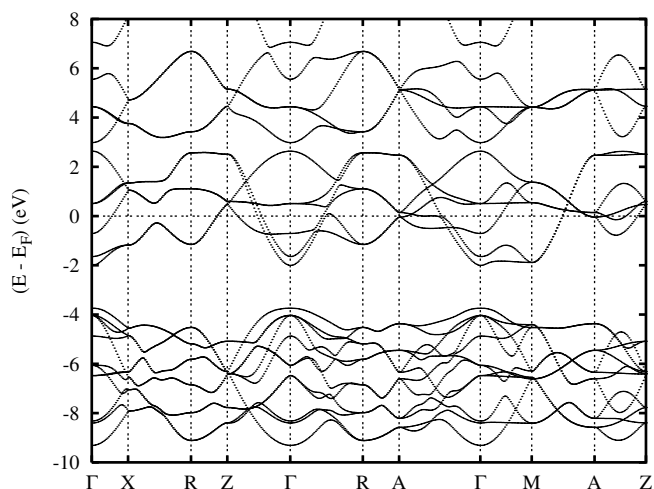
Figure 3. Electronic bands of hypothetical rutile MoO_2 along selected symmetry lines within the first Brillouin zone of the simple tetragonal lattice, shown in figure 4(a).
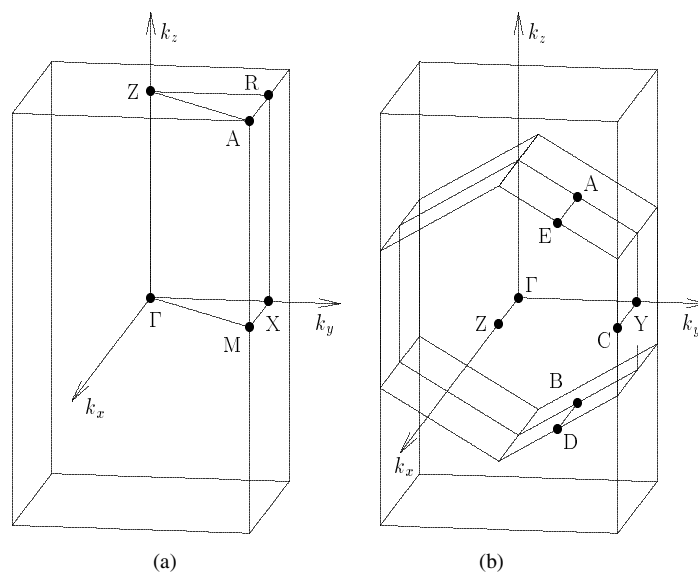

Figure 4. First Brillouin zones of the (a) simple tetragonal and (b) simple monoclinic lattices. Backfolding of the tetragonal Brillouin zone implies the following transformation of high-symmetry points: $X_T \rightarrow Y_M, Z_M$; $M_T \rightarrow C_M$; $Z_T \rightarrow Y_M$; $R_T \rightarrow \Gamma$; $A_T \rightarrow Z_M$.

in this energy range.

The general situation is very similar for the observed monoclinic structure. The corresponding band structure along selected high-symmetry lines within the first Brillouin zone of the simple monoclinic lattice, shown in figure 4(b), as well as the total and partial densities of states are shown in figures 6 and 7. We identify the same groups of bands as before, which now extend from -8.3 to -2.5 eV, -1.8 to 3 eV and 3 to 7 eV. However, the deviations from the DOS calculated for hypothetical rutile MoO_2 are also easily stated:
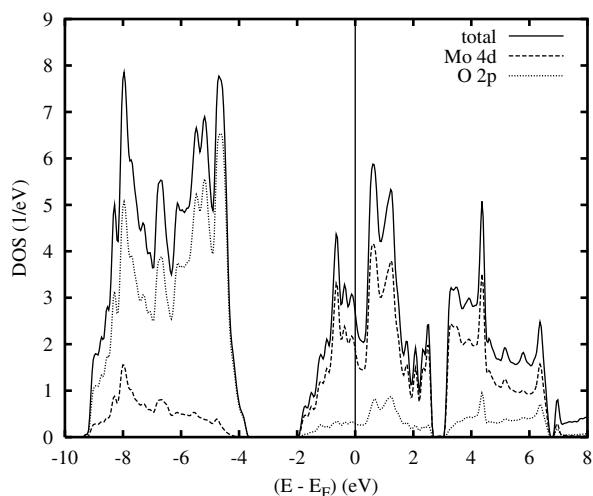
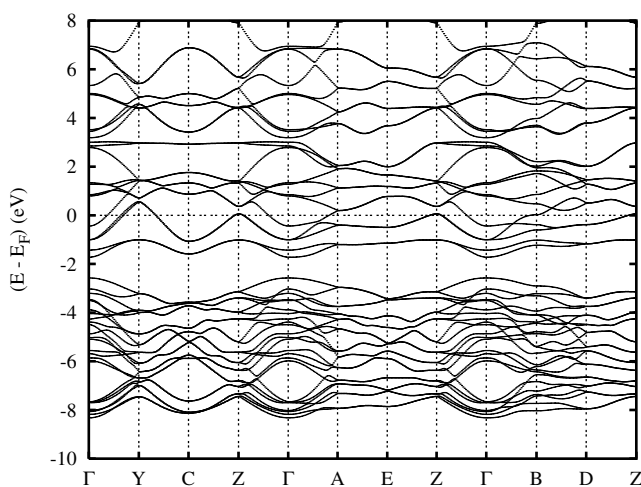**Figure 5.** Total and partial densities of states (DOS) of hypothetical rutile MoO_2 per unit cell.

Figure 6. Electronic bands of monoclinic MoO_2 along selected symmetry lines within the first Brillouin zone of the simple monoclinic lattice, shown in figure 4(b).

(i) On comparing figure 7 to figure 5 we observe an energetical upshift of the O 2p-dominated group of bands by approximately 1 eV relative to the higher-lying bands. It can be attributed to the increase of the average bond lengths between the molybdenum atoms and the oxygen ligands in the monoclinic structure by about 1%, which reduces the bonding–antibonding splitting of the σ- and π-bonded Mo 4d and O 2p states.

(ii) On going from the rutile to the monoclinic structure, the shape of the density of states, especially of the middle group of bands, displays conspicuous changes: it becomes more structured and the low- and high-energy peaks within this group have grown at expense of the central region.

(iii) From the calculations for the monoclinic structure we obtain a total density of states at the Fermi energy, $N(E_F)$, of 0.58 states eV^{-1}/f.u., which is half the value resulting from the calculations for the hypothetical rutile structure.
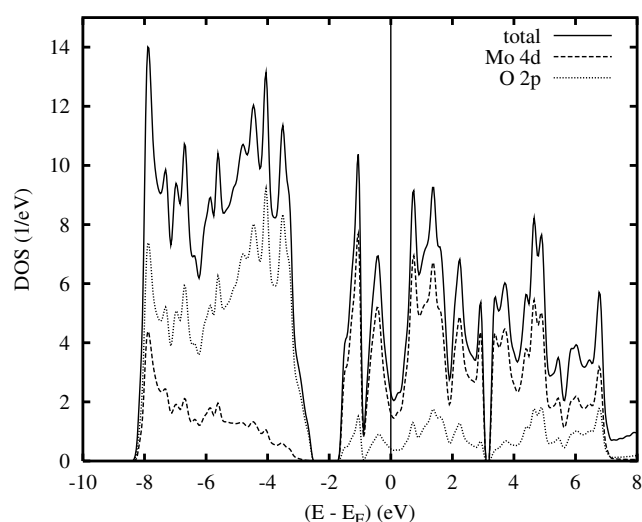
Figure 7. Total and partial densities of states (DOS) of monoclinic MoO_2 per unit cell.

The reasons underlying in particular the latter two changes become clearer from a more detailed discussion of the densities of states. To this end we display in figures 8 and 9 the partial Mo 4d DOS separated into their symmetry components. In both figures, we have included only contributions from the single molybdenum atom at or near the corner of the rutile cell and used the local rotated reference frame as visualized in figure 2. Crystal-field splitting, as expected from the fact that the metal atoms are located at the centres of distorted MoO_6 octahedra, is fully reflected by the nearly perfect energetical separation of the 4d t_{2g} and e_g groups of bands. The former states appear almost exclusively in the middle group of bands ranging from -2 to 2.7 eV and -1.8 to 3 eV, respectively, whereas the e_g states dominate the bands above 3 eV. The small but finite t_{2g}–e_g configuration mixing is a measure of octahedral distortions. Not shown are the contributions of the Mo 4d states to the low-lying oxygen bands. They are slightly larger for the e_g states, which, forming σ bonds, experience a larger overlap with the O 2p states. For the same reason, the bonding–antibonding splitting is larger for the e_g states as compared to the t_{2g} states, which give rise to π bonds.

In both figures 8 and 9 the differences among the individual symmetry components of the t_{2g} and e_g orbitals, respectively, reflect the orthorhombic site symmetry. Yet, especially the d_{xz} and d_{yz} partial DOS still bear a certain similarity, which is a consequence of the dominating tetragonal component of the crystal field. Furthermore, these two partial DOS do not change much on going from the hypothetical rutile to the monoclinic structure.

This is contrasted with by the behaviour of the $d_{x^2-y^2}$ partial DOS, which (i) deviates considerably in shape from the other t_{2g} partial DOS and (ii) displays a marked sensitivity to the structural changes. In the hypothetical rutile phase the $d_{x^2-y^2}$ states exhibit strong tendencies towards splitting into two peaks at -1 eV and above 2 eV, and the resulting depletion of the partial DOS in between contributes substantially to the DOS minimum just above the Fermi energy visible in figure 5. Nevertheless, striking differences show up on going to the monoclinic phase: the splitting of these states into two peaks increases by about 0.5 eV and the partial DOS vanishes almost completely in the interval from -1 to 2 eV, this leading to the aforementioned change in shape of the total DOS and the strong decrease of the density of states at E_F.
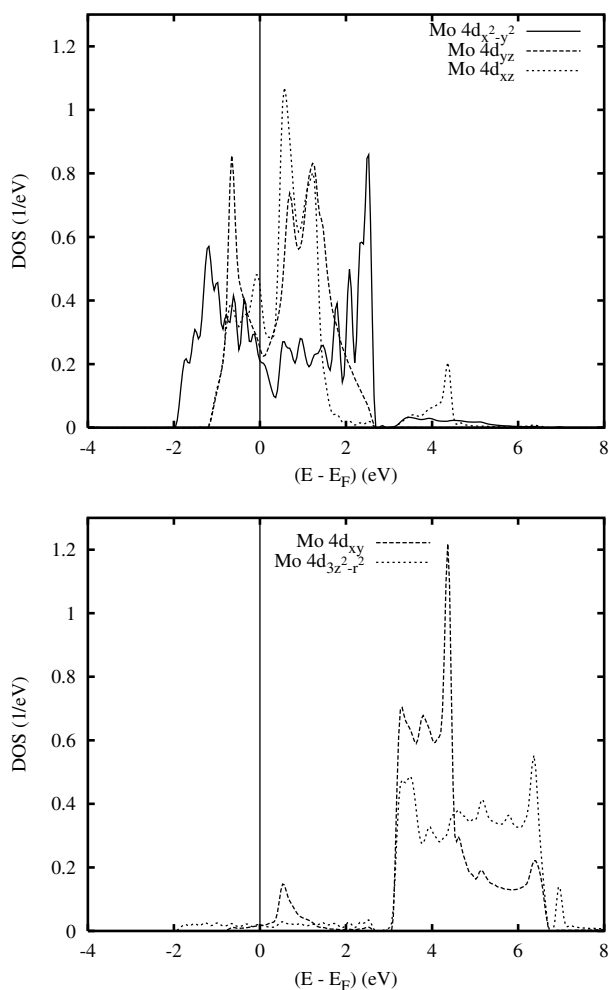
Figure 8. Partial Mo 4d t_{2g} and e_g densities of states (DOS) of hypothetical rutile MoO_2. The selection of orbitals is relative to the local rotated reference frame; see figure 2.

The drastic changes of the $d_{x^2-y^2}$ states likewise cause distinct differences of the band structure. We display in figure 10 the band structure of hypothetical rutile MoO_2 using the first Brillouin zone of the simple monoclinic lattice, shown in figure 4(b). Note that these bands result from folding back the bands calculated for the rutile structure. In the rutile calculation, those two bands which, at the Γ point, give rise to the lowest states within the t_{2g}-derived group of bands bend upwards along the lines Γ–A and Γ–B and cross the higher-lying bands. In contrast, in the observed monoclinic structure these two bands are well separated from the other states and form a split-off doublet.

All our results are in very good agreement with the molecular orbital schemes presented by Rogers *et al* [1] and Goodenough [22] as well as with the cluster and tight-binding calculations by Sasaki *et al* [25] and Burdett [27]. According to these approaches, the $d_{x^2-y^2}$ band, designated as the $d_\parallel$ band, experiences a strong bonding–antibonding splitting due to the metal–metal pairing along the tetragonal c-axis, while the π^* bands (d_{xz} and d_{yz} in our notation) stay mainly in between the two $d_\parallel$ peaks without any further splittings.
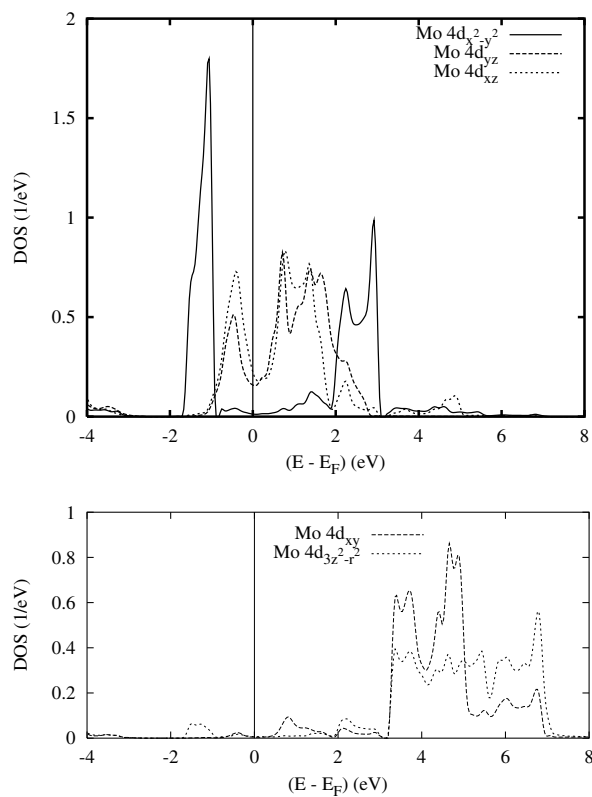
Figure 9. Partial Mo 4d t_{2g} and e_g densities of states (DOS) of monoclinic MoO_2. The selection of orbitals is relative to the local rotated reference frame.
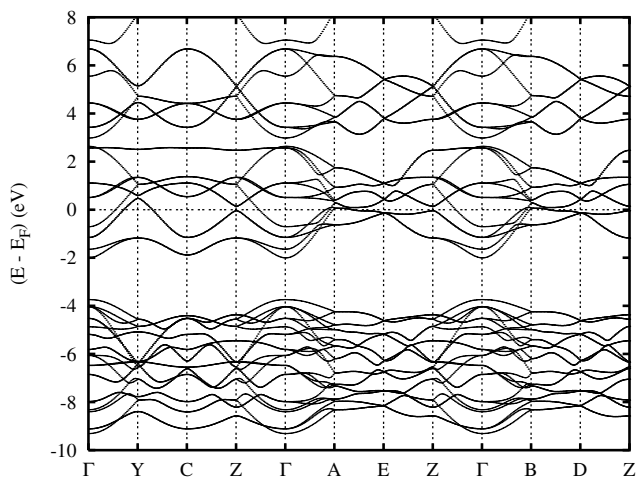

Figure 10. Electronic bands of hypothetical rutile MoO_2 along selected symmetry lines within the simple monoclinic Brillouin zone, shown in figure 4(b).

4.2. Chemical bonding

Our previous findings are supported by an analysis of the chemical bonding properties. We show in figure 11 crystal orbital overlap population (COOP) curves calculated for the hypothetical rutile structure. They display rather 'canonical' behaviour with positive (bonding)
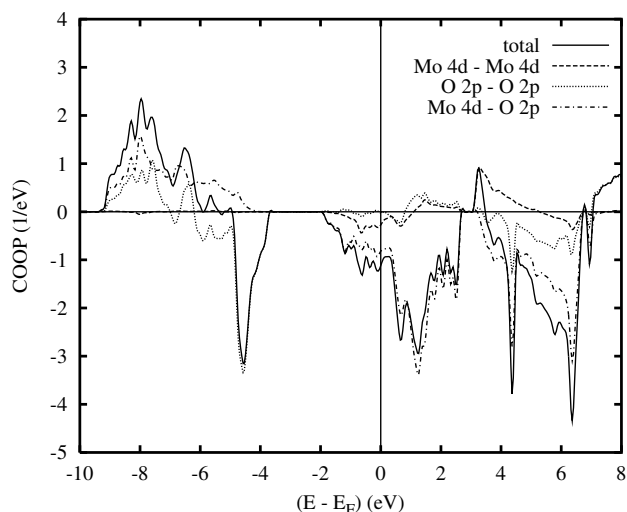
Figure 11. Total and partial crystal orbital overlap populations (COOP) of hypothetical rutile MoO$_2$.

and negative (antibonding) contributions in the low- and high-energy regions of a band [3]. In the case of the oxygen–oxygen overlap this is visible for both the oxygen- and molybdenum-dominated bands separately. Below approximately -6.5 eV we find bonding O–O bands, whereas the antibonding bands appear in the energy range between -6.5 and -3.5 eV. As a consequence, the net contribution of the occupied oxygen–oxygen bonds to the chemical stability is rather small. The same holds for the almost negligible metal–metal bonding. The dominating contribution to the chemical stability results from the overlap of Mo 4d and O 2p orbitals. The corresponding COOP curve is positive below -3.5 eV and negative only in the Mo 4d-derived bands. Hence, already from the calculations for hypothetical rutile MoO$_2$, we are able to attribute the overall chemical stability to the metal–ligand bonding.

On going to the observed monoclinic structure we observe only minor changes of the COOP, which mainly affect the metal–metal bonding. The results are shown in figure 12, where we have omitted the partial COOP curves for O 2p–O 2p as well as Mo 4d–O 2p bonding which, like the total COOP, agree closely with the curves calculated for the hypothetical rutile structure.
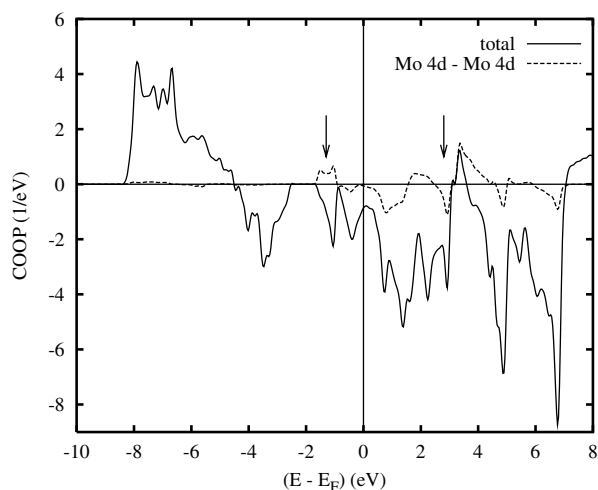

Figure 12. Total and partial crystal orbital overlap populations (COOP) of monoclinic MoO$_2$.

As expected, differences arise mainly from the bonding and antibonding Mo $4d_{x^2-y^2}$ peaks, which lead to a distinct positive contribution to the Mo–Mo curve between -2 and -1 eV and to an additional negative peak at the upper edge of the t_{2g} bands between 2 and 3 eV. These two peaks, which are indicated by arrows in figure 12, signal the increased metal–metal bonding accompanying the pairing of the atoms in the monoclinic structure. Moreover, the formation of bonding and antibonding Mo $4d_{x^2-y^2}$ states below and above the Fermi energy, respectively, increases the value of the total integrated COOP at the Fermi level (see reference [3] for details) and thus enhances significantly the stability of the compound.

4.3. Comparison to experiment

We display in figures 13 and 14 total as well as partial Mo 4d and O 2p densities of states folded with Gaussians of 0.25 and 0.5 eV width, respectively, for the occupied and unoccupied part of the spectrum. In figure 13 we have added UPS spectra as measured by Goering [15]. Good agreement of the calculated and measured curves is found. In addition, the calculated total DOS compares very well with the XPS spectra reported by Beatham and Orchard as well as those reported by Werfel and Minni [13, 14]. So far, our results are quite similar to those produced by the cluster calculations presented by Sasaki *et al* and Yoshino *et al* [25, 26]. The occupied bandwidth of ≈ 8.8 eV deduced from the experiments is close to the calculated 8.5 eV. According to Beatham and Orchard the valence band is split into a low- and a high-binding part of about 3 and 6 eV width, respectively [13]. As their UPS measurements furthermore reveal, the low-binding region falls into two main peaks at ≈ -1.5 and -0.5 eV. In the UPS spectra shown in figure 13, we find the corresponding peaks at -1.7 and -0.6 eV, whereas in the calculations they appear at -1.15 and -0.45 eV. Hence, we can state that there is almost perfect agreement for the Mo $4d_{xz}$ and $4d_{yz}$ states but an energetical upshift of the bonding Mo $4d_{x^2-y^2}$ bands of ≈ 0.45 eV relative to experiment. In passing, we note that the position of the calculated O 2p-derived bands compares very well with the optical reflectance data given by Chase as well as those given by Dissanayake and Chase, who find these states 2.5 eV below the Fermi energy [11, 12].
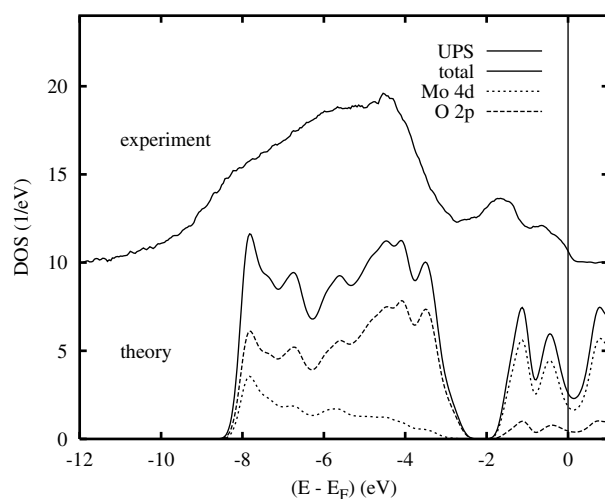

Figure 13. Total and partial densities of states (DOS) of monoclinic MoO$_2$ folded with a 0.25 eV wide Gaussian (lower set of curves) and UPS spectra (upper curve; from reference [15]).
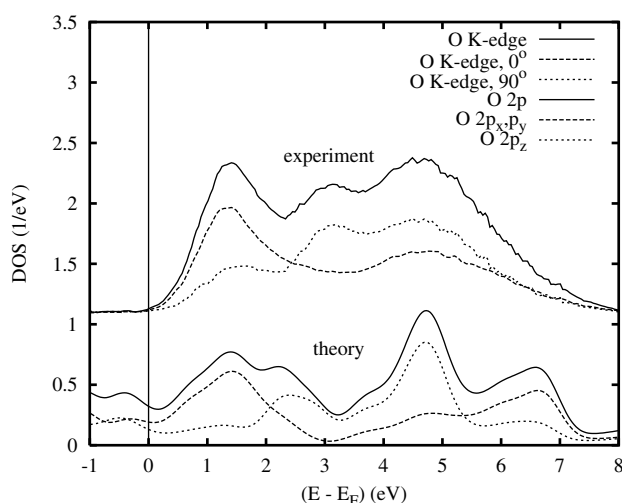
Figure 14. Partial O 2p densities of states (DOS) of monoclinic MoO_2 folded with a 0.5 eV wide Gaussian (lower set of curves) and XAS O K edge spectra (upper set of curves; from reference [16]).

In figure 14 we have complemented the theoretical results with soft-x-ray absorption spectra as measured by Müller [16]. In order to probe the angular dependence, in these experiments the polarization vector E was oriented either parallel ($\phi = 90°$) or else perpendicular ($\phi = 0°$) to the rutile c-axis. In the former case, dipole selection rules allow for transitions from the O 1s to the O $2p_z$ state. In contrast, for E perpendicular to the c-axis, transitions to the O $2p_x$ and $2p_y$ states may occur. We have added the partial DOS of the corresponding final states in figure 14. However, note that the curve marked O $2p_x$, p_y comprises only the mean average of these orbitals, since the component perpendicular to E is not seen in experiment. For the same reason, the curve marked O 2p actually contains the contribution from $\frac{1}{2}(p_x + p_y) + p_z$. Again, there is an overall good agreement between experiment and theory. This holds not only for the positions of most peaks, but also for their relative intensity as well as their angular dependence. We draw attention especially to the suppression, on increase of the angle ϕ, of the peak due to the Mo $4d_{xz}$ and $4d_{yz}$ bands at 1.2 eV. Still, this good agreement is contrasted with two distinct deviations. First, the broad maximum at 6.6 eV in the calculated DOS, which results from the O $2p_x$ and $2p_y$ states, is not seen in experiment. According to the molybdenum partial DOS shown in figure 9, this maximum originates mainly from the Mo $4d_{3z^2-r^2}$ orbitals. Second, the maximum in the O $2p_z$ partial DOS at ≈ 2.4 eV is located at ≈ 3.1 eV in the XAS spectra. From a comparison to the partial Mo 4d DOS, in figure 9, we attribute this maximum to the antibonding $d_{x^2-y^2}$ orbitals. Their energetical downshift relative to experiment adds to the aforementioned deviation of about 0.45 eV of the corresponding bonding states. It thus seems that the calculations underestimate the bonding–antibonding splitting of the Mo $4d_{x^2-y^2}$ states by approximately 1 eV.

4.4. The Fermi surface

So far our results have established full agreement of the molecular orbital picture sketched by Rogers *et al* [1] as well as by Goodenough [22] with state-of-the-art electronic structure calculations in that they relate the splitting of the Mo $4d_{x^2-y^2}$ states into two peaks to the metal–metal pairing in the monoclinic structure. However, we still lack a deeper understanding of the

mechanisms driving this scenario including the R-point instability of the hypothetical rutile structure compatible with the experimentally observed monoclinic structure. For this reason we will proceed in two steps and investigate in this and the subsequent subsection in more detail the Fermi surface as well as the symmetry character of the electronic states near the Fermi energy.

Cuts through the Fermi surface parallel to the {100} and {110} planes which were calculated for the hypothetical rutile structure are shown in figures 15, 16, and 17. They contain the Γ–X–Z–R, Γ–M–Z–A, and X–M–R–A planes, respectively, which are the vertical borders of the irreducible wedge of the first Brillouin zone; see figure 4(a). The interpretation of these figures is greatly facilitated by combining them with the band structure shown in figure 3. From this, we recognize electron- and hole-like regions near the Γ and Z points, respectively. Along the line Z–A, as given in figure 16, several electron-like pockets interpenetrate. Of course, the most striking features are the two flat Fermi surface sheets in figure 16 halfway between the lines Γ–M and Z–A, which hardly depend on the lateral position of the k-vector. These flat sheets show up likewise in figures 15 and 17 where, however, they extend only over part of the respective horizontal lines. Gathering together the information from figures 15 to 17, we conclude that the Fermi surface forms two almost perfect {001} planes at height $\pi/(2c)$, which have rather small interruptions above the X points. These planes give rise to Fermi surface nesting with the z-component of the wave vector being $q_z = \pi/c$.
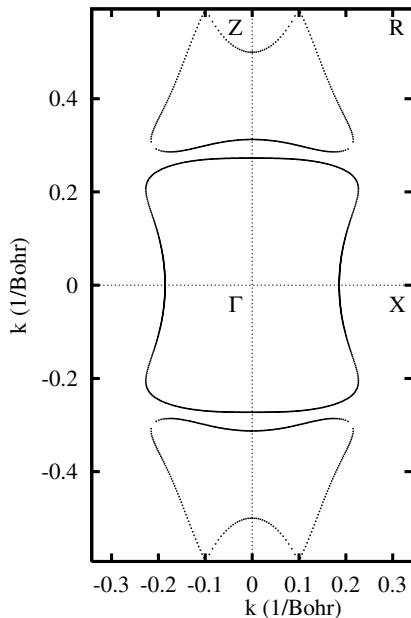

Figure 15. A {100} cut through the Fermi surface of hypothetical rutile MoO$_2$.

However, the lateral components of the q-vector are still unspecified: any wave vector with $q_z = \pi/c$ transforms the flat sheets into themselves irrespective of the other two components. In order to attempt full specification of the wave vector we have to take the remaining portions of the Fermi surface into account. In doing so, we might deduce further nesting from the nearly rectangular sheet centred about the Γ point in figure 15, which has a small narrowing in the basal plane of the Brillouin zone. This part of the Fermi surface favours wave vectors with the x- or y-component equal to π/a. However, the Fermi surface area visible in figure 15 is much smaller than the previously discussed twofold flat {001} sheet. To conclude, Fermi surface considerations do not allow one to uniquely determine a nesting vector and, hence, cannot
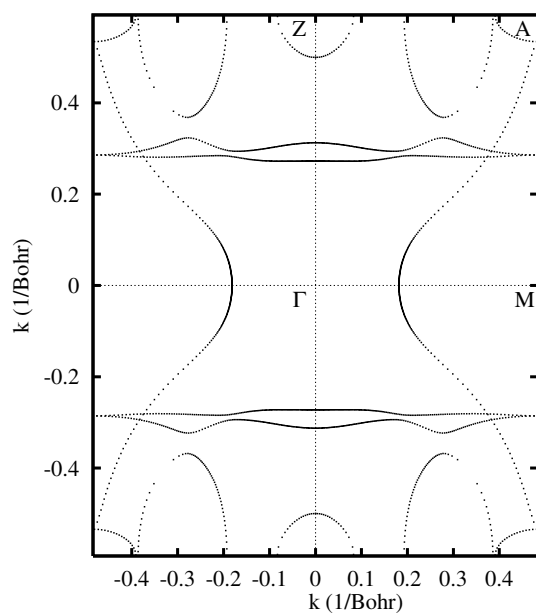
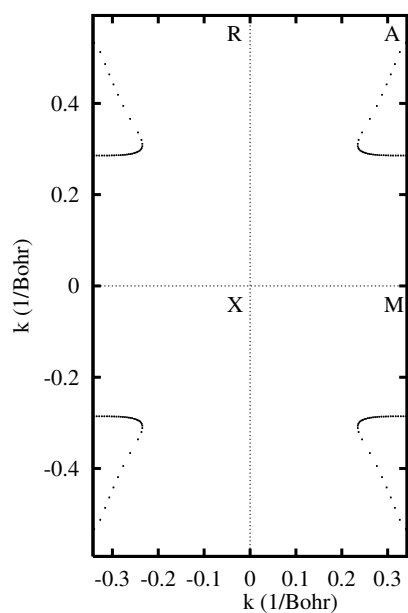**Figure 16.** A {110} cut through the Fermi surface of hypothetical rutile MoO_2.

Figure 17. A {100} cut through the Fermi surface of hypothetical rutile MoO_2.

explain the instability of the hypothetical rutile structure against the observed monoclinic structure.

Although somewhat disappointing, this result fits into the broader context of the neighbouring dioxides, which likewise prefer the monoclinic over the rutile structure. Since they comprise d^1, d^2, and d^3 configurations, a Fermi surface instability is hard to imagine as a common mechanism for all these compounds. Similar considerations led Goodenough to rule out a Jahn–Teller effect as a major source for the crystal structure characteristics of the early transition metal dioxides [46].

4.5. Symmetry analysis of the band structure

Still keeping the conspicuous nesting with $q_z = \pi/c$ in mind, we turn to the symmetry analysis of the electronic band structure, which complements and adds detail to the previous discussion of the partial densities of states. To this end we display in figures 18, 19, and 20 the electronic bands in the narrow energy range from -2.5 to 3.5 eV about the Fermi energy in a special representation. In all three figures, each band at each k-point is given a bar whose length is a measure for the contribution from a specified orbital. Note that in doing this we again referred to the local frame of reference. Hence, figures 18 to 20 correspond to the partial Mo 4d t_{2g} DOS shown in figure 8, which likewise made use of the local reference frame.
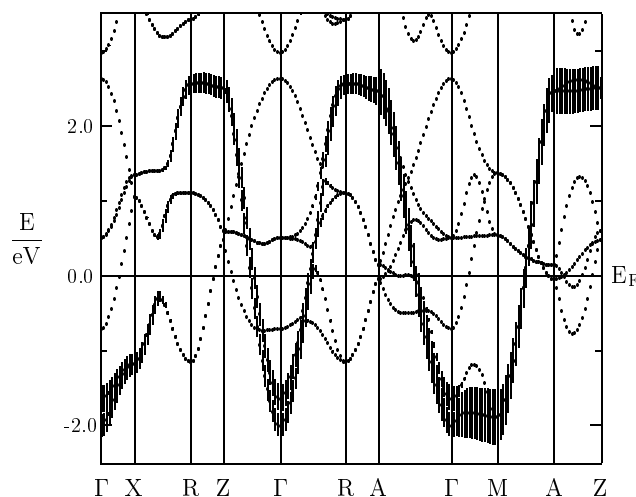

Figure 18. Weighted electronic bands of hypothetical rutile MoO$_2$. For each band the width of the bar indicates the contribution from the $4d_{x^2-y^2}$ orbital of the Mo atom at $(0, 0, 0)$ relative to the local rotated reference frame.

In figure 18 we observe a strong dispersion of the Mo $4d_{x^2-y^2}$-derived bands along all lines parallel to Γ–Z, whereas the dispersion perpendicular to this line is almost vanishing. Recalling the fact that the local x-axes point along the rutile c-axis, we attribute the strong dispersion in this direction to the overlap of the $d_{x^2-y^2}$ orbitals at metal sites neighbouring in the z-direction. The large bandwidth thus reflects the small metal–metal distance in this direction. The splitting of these states especially along the lines Γ–M and A–Z is caused by their overlap across the neighbouring octahedral chains, i.e. the inter-chain interaction. Since the distance between chains across the diagonal of the rutile basal plane is smaller than that parallel to the $\langle 100 \rangle$ axes, this splitting is much reduced along the lines Γ–X, R–Z, and R–A.

The Mo $4d_{yz}$-derived bands are highlighted in figure 20. They show a large dispersion in all directions with the bandwidth being somewhat reduced as compared to that of the $d_{x^2-y^2}$-derived bands. Worth mentioning is the rather large splitting at the Γ point. It is a consequence of the underlying body-centred tetragonal (bct) lattice formed by the metal atoms, and results from backfolding the bands from the Brillouin zone of the bct lattice to the smaller one of the simple tetragonal lattice. This effect is visible especially in the bands along the lines connecting the Γ point to the X, M, A, and Z points, respectively. Since the formation of the d_{yz} bands results from σ-type overlap of these orbitals across the tetragonal lattice and the lattice constants a are larger than the lattice constant c, the overlap is reduced as compared to that of the $d_{x^2-y^2}$ orbitals and so is the dispersion.
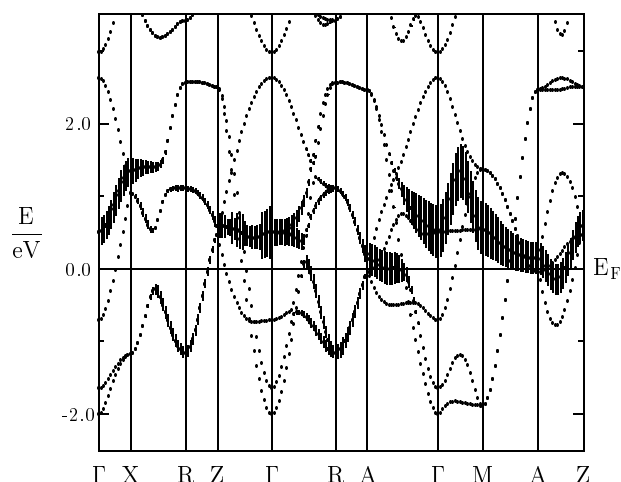
Figure 19. Weighted electronic bands of hypothetical rutile MoO$_2$. For each band the width of the bar indicates the contribution from the 4d$_{xz}$ orbital of the Mo atom at (0, 0, 0) relative to the local rotated reference frame.

Figure 20. Weighted electronic bands of hypothetical rutile MoO$_2$. For each band the width of the bar indicates the contribution from the 4d$_{yz}$ orbital of the Mo atom at (0, 0, 0) relative to the local rotated reference frame.
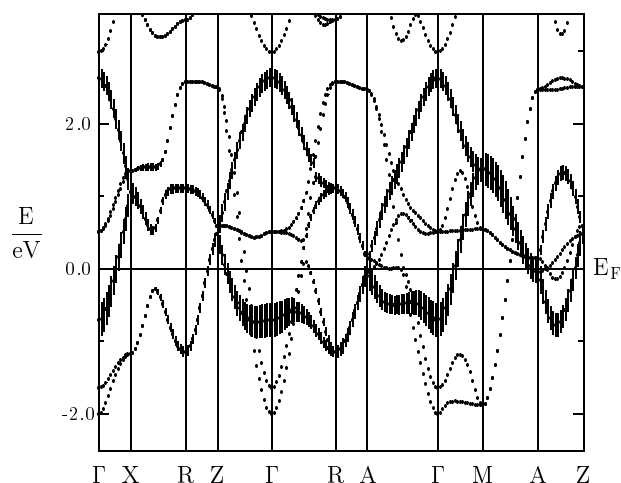
Finally, Mo 4d$_{xz}$ bands display the smallest dispersion. This is due to the fact that these orbitals induce no substantial σ-type overlap with neighbouring metal atoms but take part in the (albeit small) coupling between the octahedral chains.

However, the most important result of the previous band-structure analysis consists of the fact that all three bands disperse without any substantial hybridization with each other. The only exception worth mentioning stems from the hybridization of the d$_{x^2-y^2}$ bands with the d$_{yz}$- and d$_{xz}$-derived bands in the middle of the symmetry line X–R. Otherwise there are only some degeneracies of the d$_{yz}$ and d$_{xz}$ bands, e.g. along the lines Γ–R and R–A, which, however, do not induce large shifts of the bands near the Fermi energy. Hence, the three t$_{2g}$-derived bands behave almost completely independently.

This fact has important implications for the interpretation of the Fermi surface results, since it allows one to uniquely assign each section of the Fermi surface to a single t_{2g} band. First, we attribute the almost perfect twofold flat Fermi surface in figures 15 to 17 exclusively to the $d_{x^2-y^2}$ bands. The aforementioned interruptions of this sheet above the X points can be clearly connected to the hybridization of the $d_{x^2-y^2}$ bands with the d_{yz}- and d_{xz}-derived bands along the symmetry line X–R. It pushes the bands away from the Fermi energy and thereby suppresses the Fermi surface portions in this k-space region. Nevertheless, the size of these disruptions is rather limited and, hence, does not diminish the predominant influence of the nesting with $q_z = \pi/c$.

The d_{yz} bands, which cut the Fermi energy along the lines Γ–X and Γ–M, are responsible for those parts of the Fermi surface which are perpendicular to the basal plane. In particular, the vertical edges of the rectangle centred about the Γ point as seen in figure 15 can be attributed to these bands.

4.6. Embedded Peierls-type instability

The results of the previous two subsections can be summarized to the statement that, were it not for the π^* bands, we would end up with an assembly of weakly coupled Mo chains. The nesting resulting from the twofold flat sheets should then give rise to a Peierls-type instability of the $d_\parallel$ bands, which is accompanied by a modulation of the metal-atom positions along the rutile c-axis with a wave-vector component $q_z = (0, 0, \pi/c)$, i.e. a doubling of the c-axis and a metal–metal pairing along this axis. Still, it remains to be demonstrated that this general picture is not qualitatively altered by the presence of a three-dimensional background of π^* electrons and that the increase in bonding–antibonding splitting of the Mo $4d_{x^2-y^2}$ ($d_\parallel$) states on going from the hypothetical rutile to the observed monoclinic structure as seen in figures 8 and 9 can be understood within the just-sketched framework of a Peierls-like scenario. To this end we visualize, in particular, the changes of the $d_{x^2-y^2}$ bands by using the same special representation of the band structure as in figures 18 to 20 above. We thus again attach to each band at each k-point a bar which reflects the contribution from the $d_{x^2-y^2}$ orbital.

We start the discussion by displaying in figure 21 the electronic structure of hypothetical rutile MoO_2 in the narrow energy range from −2.5 to 3.5 eV about the Fermi energy, represented along the high-symmetry lines within the first Brillouin zone of the simple monoclinic lattice, shown in figure 4(b). In the same way as figure 10 was deduced from figure 3, figure 21 can thus be constructed from figure 18 by folding the bands back from the simple tetragonal to the simple monoclinic Brillouin zone. As was already discussed in connection with figure 18, there is a strong dispersion along the lines Γ–A, E–Z, Γ–B, and D–Z, which have components perpendicular to the rutile basal plane and correspond to half of the line Γ–R and half of the line X–A of the tetragonal Brillouin zone. In contrast, the dispersion parallel to the rutile basal plane is almost completely suppressed, with the bands staying at energies either well below or above the Fermi energy. Exceptions include the lines A–E and B–D, where the Mo $4d_{x^2-y^2}$ states, while showing an almost vanishing dispersion, are found right at E_F. This is connected with the fact that these lines extend *within* the planes at height $\pi/(2c)$, which, as has been discussed in section 4.4, contain the characteristic twofold flat Fermi surface sections accompanying the rutile structure. Hence, the lines A–E and B–D just extend through the dominating part of the rutile Fermi surface.

The situation changes completely when we turn to monoclinic MoO_2, for which we show the analogous band structure in figure 22. In the monoclinic structure the occupied and unoccupied Mo $4d_{x^2-y^2}$ bands along the lines Γ–A–E–Z and Γ–B–D–Z have moved by as much as ≈2 eV downward and upward, respectively, relative to their positions in hypothetical

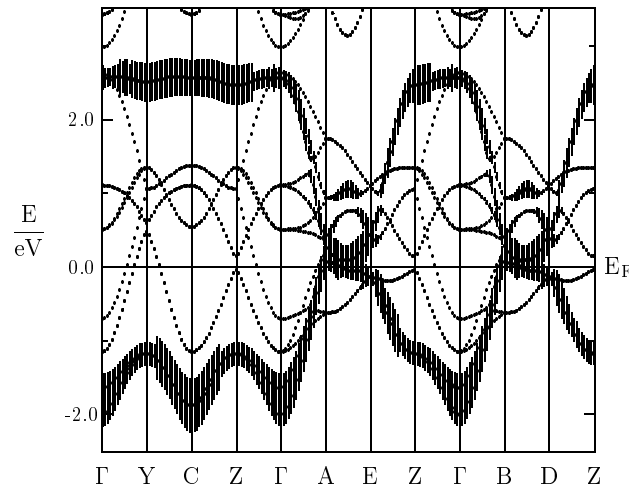**Figure 21.** Weighted electronic bands of hypothetical rutile MoO_2 along selected symmetry lines within the simple monoclinic Brillouin zone, shown in figure 4(b). The meaning of the widths of the bars is the same as in figure 18.
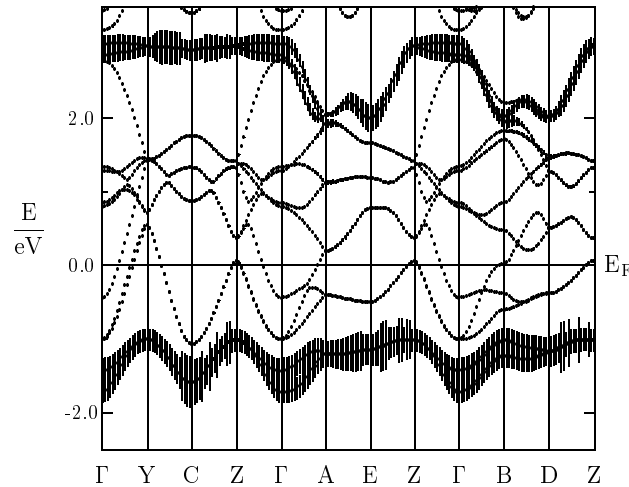

Figure 22. Weighted electronic bands of monoclinic MoO_2. The meaning of the widths of the bars is the same as in figure 18.

rutile MoO_2. This leads, in particular, to the formation of the split-off double band at the lower edge of the t_{2g} group, which we mentioned already at the end of section 4.1. As a consequence of these drastic band-shifts, the Fermi surface due to the $d_{x^2-y^2}$ states has vanished completely. Moreover, the downshifts of the $d_{x^2-y^2}$ states along the lines Γ–A–E–Z and Γ–B–D–Z cause a considerable lowering of the total energy and, hence, a stabilization of the monoclinic structure. In contrast, all other bands in the energy range from −2 to 2.5 eV, which according to the analysis given in section 4.5 are mainly of Mo $4d_{xz}$ and $4d_{yz}$ character, experienced only minor changes and maintain the metallic conductivity. To conclude, we have indeed arrived at a Peierls-like scenario for the $d_∥$ bands, which occurs without any visible disturbance by the three-dimensional background of $π^*$ electrons.

Finally, in order to check the relative importance of the metal–metal dimerization and the zigzag-like lateral displacement of the metal atoms, we complement the previous results with figure 23, which likewise corresponds to a hypothetical crystal structure. However, in this structure, we assumed a monoclinic lattice and included the metal–metal dimerization but ignored the zigzag-like lateral displacement (as well as the lattice strain). Obviously, the complete separation of the bonding and antibonding $d_\parallel$ bands in figure 23 reveals the dominant influence of the metal–metal dimerization on the electronic structure. Yet, the dispersion, especially of the bonding part of the $d_\parallel$ bands, is still about twice as large as in the observed monoclinic structure; see figure 22. Since according to analogous calculations the influence of the lattice strain on the band structure is rather small, we attribute the change in dispersion to the zigzag-like displacement of the Mo atoms. This is due to the fact that the zigzag motion of the metal atoms shifts the $d_{x^2-y^2}$ orbitals away from the rutile *c*-axis and thus diminishes the overlap of the $d_\parallel$ orbitals along the chains. In this respect the zigzag motion assists the metal–metal dimerization in separating the bands. This behaviour is quite similar to the situation in V_2O_5, where the zigzag-like distortion of the characteristic V–O double chains diminishes overlap along the chains and substantially reduces the dispersion of the split-off conduction bands [43].
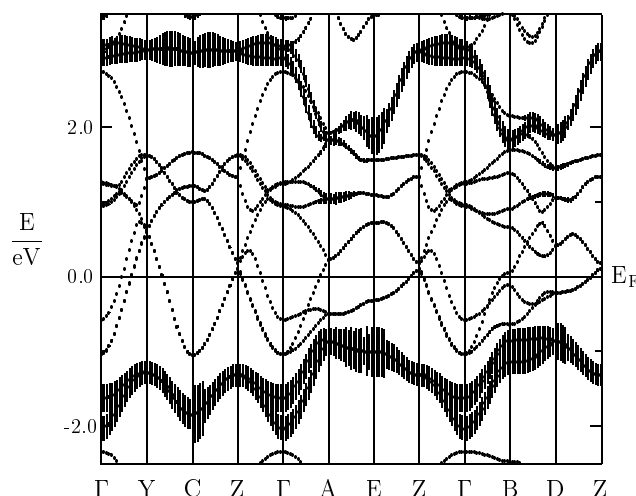

Figure 23. Weighted electronic bands of monoclinic MoO_2 with only the dimerization included. The meaning of the widths of the bars is the same as in figure 18.

5. Conclusions

The present first-principles ASW study of both the monoclinic and a hypothetical rutile structure of MoO_2 revealed a striking sensitivity of the Mo 4d $d_\parallel$ states to structural changes. While in the high-symmetry structure these bands display a quasi-one-dimensional dispersion parallel to the rutile *c*-axis, they experience strong splitting of ≈ 4 eV into bonding and antibonding branches due to the metal–metal dimerization characteristic of the monoclinic structure. At the same time they embrace the isotropically dispersing π^* states, which stay rather inert and maintain the metallic conductivity. Hybridization between the $d_\parallel$ and π^* states is only limited. As a consequence of the breakdown of the $d_\parallel$ dispersion, the almost perfect Fermi surface nesting of these bands on sheets bisecting the line Γ–Z is completely destroyed.

We thus interpret the monoclinic structure as resulting from a Peierls-type instability of the quasi-1D $d_\parallel$ bands in the presence of an isotropic background of π^* electrons.

Although we find in general good agreement with recent UPS and XAS data, distinct deviations occur for the positions of the bonding and antibonding $d_\parallel$ states. Due to the imperfections of the LDA, their splitting is underestimated by ≈ 1 eV in the calculations for metallic MoO_2. The same situation has been reported for VO_2 in its monoclinic insulating phase, where the incomplete separation of the $d_\parallel$ bands within the LDA causes a slight semimetallic-like overlap of the bonding $d_\parallel$ and the π^* bands, and the opening of the optical band gap is just missed [47, 48]

Naturally, the observed scenario of an embedded Peierls-type instability in MoO_2 has considerable implications for the construction of model Hamiltonians aiming at a description of the early transition metal dioxides, in particular, of the neighbouring oxides VO_2 and CrO_2, as well as their low-temperature instabilities.

Acknowledgments

References

[1] Rogers D B, Shannon R D, Sleight A W and Gillson J L 1969 *Inorg. Chem.* **8** 841
[2] Mattheiss L F 1976 *Phys. Rev.* B **13** 2433
[3] Eyert V 1997 Electronic structure calculations for crystalline materials *Density Functional Methods: Applications in Chemistry and Materials Science* ed M Springborg (Chichester: Wiley) pp 233–304
[4] Bolzan A A, Fong C, Kennedy B J and Howard C J 1997 *Acta Crystallogr.* B **53** 373
[5] Morin F J 1959 *Phys. Rev. Lett.* **3** 34
[6] Marinder B-O 1962 *Ark. Kemi* **19** 435
[7] Cox P A 1992 *Transition Metal Oxides* (Oxford: Clarendon)
[8] Shapiro S M, Axe J D, Shirane G and Raccah P M 1974 *Solid State Commun.* **15** 377
[9] Pynn R, Axe J D and Thomas R 1976 *Phys. Rev.* B **13** 2965
[10] Cheetham A K and Rao C N R 1976 *Acta Crystallogr.* B **32** 1579
[11] Chase L L 1974 *Phys. Rev.* B **10** 2226
[12] Dissanayake M A K L and Chase L L 1978 *Phys. Rev.* B **18** 6872
[13] Beatham N and Orchard A F 1979 *J. Electron Spectrosc. Relat. Phenom.* **16** 77
[14] Werfel F and Minni E 1983 *J. Phys. C: Solid State Phys.* **16** 6091
[15] Goering E 1996 *PhD Thesis* Universität Augsburg
[16] Müller O 1996 *PhD Thesis* Universität Augsburg
[17] Vol'skiĭ E P and Teplinskiĭ V M 1973 *Sov. Phys.–JETP* **36** 550
[18] Vol'skiĭ E P and Teplinskiĭ V M 1975 *Sov. Phys.–JETP* **42** 373
[19] Vol'skiĭ E P, Gapotchenko A G, Itskevich E S and Teplinskiĭ V M 1979 *Sov. Phys.–JETP* **49** 848
[20] Teplinskiĭ V M 1980 *Sov. Phys.–JETP* **51** 995
[21] Klimm S 1997 *PhD Thesis* Universität Augsburg
[22] Goodenough J B 1971 Metallic oxides *Progress in Solid State Chemistry* ed H Reiss (Oxford: Pergamon) pp 145–399
[23] Kuz'min E V and Ovchinnikov S G 1977 *Sov. Phys.–Solid State* **19** 1752
[24] Sasaki T A and Kiuchi K 1981 *Chem. Phys. Lett.* **84** 356
[25] Sasaki T A, Soga T and Adachi H 1982 *Phys. Status Solidi* b **113** 647
[26] Yoshino H, Shimikoshi K and Miyazaki E 1985 *J. Electron Spectrosc. Relat. Phenom.* **36** 269
[27] Burdett J K 1985 *Inorg. Chem.* **24** 2244
[28] Hoffmann R 1988 *Solids and Surfaces: a Chemist's View of Bonding in Extended Structures* (New York: VCH)
[29] Eyert V and Matar S F 1996 unpublished

[30] Sorantin P I and Schwarz K 1992 *Inorg. Chem.* **31** 567
[31] Magnéli A and Andersson G 1955 *Acta Chim. Scand.* **9** 1378
[32] Brandt B G and Skapski A C 1967 *Acta Chim. Scand.* **21** 661
[33] Ghedira M, Do-Dinh C, Marezio M and Mercier J 1985 *J. Solid State Chem.* **59** 159
[34] Vincent H and Marezio M 1989 On structural aspects of molybdenum bronzes and molybdenum oxides in relation to their low-dimensional transport properties *Low-Dimensional Electronic Properties of Molybdenum Bronzes and Oxides* ed C Schlenker (Dordrecht: Kluwer Academic) pp 49–86
[35] Hohenberg P and Kohn W 1964 *Phys. Rev.* **136** B864
[36] Kohn W and Sham L J 1965 *Phys. Rev.* **140** A1133
[37] Williams A R, Kübler J and Gelatt C D Jr 1979 *Phys. Rev.* B **19** 6094
[38] Eyert V 1991 *PhD Thesis* Technische Hochschule Darmstadt
[39] Kübler J and Eyert V 1992 Electronic structure calculations *Electronic and Magnetic Properties of Metals and Ceramics (Materials Science and Technology Series vol 3A)* ed K H J Buschow, 1991–96 Series ed R W Cahn, P Haasen and E J Kramer (Weinheim: VCH) pp 1–145
[40] Eyert V 2000 Basic notions and applications of the augmented spherical wave method *Int. J. Quantum Chem.* **77** 1007 (Special Issue: *Electronic Structure of Materials* ed M Defranceschi)
[41] Andersen O K 1975 *Phys. Rev.* B **12** 3060
[42] Andersen O K, Postnikov A V and Savrasov S Yu 1992 The muffin-tin orbital point of view *Applications of Multiple Scattering Theory to Materials Science (MRS Symp. Proc. No 253)* ed W H Butler, P H Dederichs, A Gonis and R L Weaver (Pittsburgh, PA: Materials Research Society) p 37
[43] Eyert V and Höck K-H 1998 *Phys. Rev.* B **57** 12 727
[44] Eyert V 1996 *J. Comput. Phys.* **124** 271
[45] Eyert V, Siberchicot B and Verdaguer M 1997 *Phys. Rev.* B **56** 8959
[46] Goodenough J B 1960 *Phys. Rev.* **117** 1442
[47] Wentzcovitch R M, Schulz W W and Allen P B 1994 *Phys. Rev. Lett.* **72** 3389
[48] Eyert V 1998 Octahedral deformations and metal–insulator transition in transition metal chalcogenides *Habilitation Thesis* Universität Augsburg